HHS Public Access

Author manuscript

NMR Biomed. Author manuscript; available in PMC 2019 December 01.

Published in final edited form as:

NMR Biomed. 2018 December ; 31(12): e4009. doi:10.1002/nbm.4009.

3.0T relaxation time measurements of human lymph nodes in adults with and without lymphatic insufficiency: implications for magnetic resonance lymphatic imaging

Rachelle Crescenzi[1,*], **Paula M. Donahue**[2,3], **Vaughn G. Braxton**[1], **Allison O. Scott**[1], **Helen B. Mahany**[1], **Sarah K. Lants**[1], and **Manus J. Donahue**[1,4,5,6]

[1]Vanderbilt University Medical Center, Radiology and Radiological Sciences, Nashville, TN, USA

[2]Physical Medicine and Rehabilitation, Vanderbilt University Medical Center, Nashville, TN, USA

[3]Vanderbilt Dayani Center for Health and Wellness, Nashville, TN, USA

[4]Neurology, Vanderbilt University Medical Center, Nashville, TN, USA

[5]Psychiatry, Vanderbilt University Medical Center, Nashville, TN, USA

[6]Physics and Astronomy, Vanderbilt University, Nashville, TN, USA

Abstract

Purpose: To quantify 3.0T (i) T_1 and T_2 relaxation times of *in vivo* human lymph nodes (LNs), and (ii) LN relaxometry differences between healthy LNs and LNs from patients with lymphatic insufficiency secondary to breast cancer treatment-related lymphedema (BCRL).

Materials and Methods: MR relaxometry was performed over bilateral axillary regions at 3.0T in healthy female controls (105 LNs from 20 participants) and patients with BCRL (108 LNs from 20 participants). Quantitative T_1 maps were calculated using a multi-flip-angle (20, 40, 60 degrees) method with B_1-correction (dual-TR method, TR_1/TR_2=30/130 ms), and T_2 maps using a multi-echo (TE=9–189 ms; 12 ms intervals) method. T_1 and T_2 were quantified in the LN cortex and hilum. A Mann-Whitney U-test was applied to compare LN relaxometry values between patients and controls (significance: two-sided $p<0.05$). Linear regression was applied to evaluate how LN relaxometry varied with age, BMI, and clinical indicators of disease.

Results: LN substructure relaxation times (mean ± standard deviation) in healthy controls were: T_1 cortex=1435±391 ms, T_1 hilum=714±123 ms; T_2 cortex=102±12 ms, and T_2 hilum=119±21 ms. T_1 of the LN cortex was significantly reduced in the contralateral axilla of BCRL patients compared to the axilla on the surgical side ($p<0.001$) and compared to bilateral control values ($p<0.01$). The LN cortex T_1 asymmetry discriminated cases vs. controls ($p=0.004$) in a multiple linear regression, accounting for age and BMI.

Conclusion: Human 3.0T T_1 and T_2 relaxation times in axillary LNs were quantified for the first time *in vivo*. Measured values are relevant for optimizing acquisition parameters in anatomical

[*]**Corresponding author**: Rachelle Crescenzi, Vanderbilt University Institute of Imaging Science, 1161 21st Ave South, Nashville, TN, USA, Tel: +1 615.343.0466, Fax: +1 615.322.0734, rachelle.crescenzi@vumc.org.

lymphatic imaging sequences, and can serve as a reference for novel functional and molecular LN imaging methods that require quantitative knowledge of LN relaxation times.

Keywords

relaxometry; breast cancer; cancer therapy responses; metastases

Introduction

The lymphatic system is a central component of the human circulatory system, serving to circulate and process 3-5 liters of lymphatic fluid daily in adults[1]. Healthy lymphatic function facilitates immune responses, interstitial fluid clearance, and absorption and transport of fatty acids[2]. Lymphatic dysfunction has well-known relevance to cancer metastasis[3] and is a common comorbidity associated with cancer therapies[4]. Despite growing recognition of the lymphatics in human pathology[5], magnetic resonance imaging (MRI) methods have generally not been developed to visualize lymphatic circulation and associated lymph node (LN) structure or function to the same degree as they have to visualize the blood circulation.

More specifically, approximately 500-700 LNs exist throughout the human body, which function to process and clear metastatic cells and pathogens transported from peripheral tissues[6]. LNs typically range in size from 1-10 mm diameter and receive lymphatic fluid from multiple afferent lymph vessels that enter the cortex. The LN cortex is a region rich in B-cell (superficial cortex) and T-cell (paracortex) lymphocytes that process lymph fluid; lymphatic fluid exits the LN via an efferent vessel at the location of the hilum. In the context of cancer, LN cortex hypertrophy and ablation of the hilum is common in metastatic disease[7], although LN structure alone remains an incomplete indicator of metastatic disease and lymphatic functioning[8].

Further, the response of LN structure and function to cancer treatments is incompletely characterized. Patients receiving LN removal procedures, one of the most common cancer therapies for disease staging, are at risk for developing secondary lymphedema[9]: an incurable condition affecting the body's ability to process lymphatic fluid resulting in swelling of the dependent tissues and requiring lifetime management[10]. Such patients represent an important candidate population to evaluate how LN anatomy and function change when lymphatic processing capacity is compromised under known conditions.

MRI is a versatile modality for characterizing LN structure and function, however standard protocols for clinical LN imaging remain underdeveloped: even the fundamental MRI parameters, longitudinal (T_1) and transverse (T_2) relaxation times, needed for optimizing signal contrast, have not been rigorously measured in human LNs *in vivo*. MR relaxation times are reported in *ex vivo* healthy axillary LNs using 7.0T MRI[11], however *ex vivo* 7.0T findings cannot be generalized to the *in vivo* setting at a clinical field strength of 3.0T. It also remains unclear how T_1 and T_2 relaxation times change in response to lymphatic dysfunction, and whether these parameters may provide markers of LN health.

Therefore, the purpose of this work is to measure *in vivo* T_1 and T_2 relaxation times of axillary LN substructures, specifically the LN cortex and hilum, at a clinical field strength of 3.0T in volunteers with no history of cancer, active infection, or axillary LN impairment, and to compare these values to those in LN substructures of patients with lymphatic mechanical insufficiency of known etiology. This information is then utilized to present a range of optimal MRI protocol parameters for axillary LN imaging and to demonstrate how such protocols may be utilized to evaluate pathological LN anatomy and relaxometry *in vivo*.

Materials and Methods

Volunteer demographics

All participants provided informed, written consent and study procedures were approved by the local Institutional Review Board (IRB). Healthy female volunteers (n=20; age=48.2±12.0 years; body-mass-index (BMI)=29.2±7.5 kg/m^2; 90% right hand dominant) with no history of lymphatic impairment, active infection, or injury to the upper extremities were enrolled. Females with breast cancer treatment-related lymphedema (BCRL; n=20 females; age=53.0±9.0 years; BMI=28.4±4.6 kg/m^2; 100% right hand dominant) were enrolled to understand if relaxation times varied in subjects with known lymphatic processing insufficiency following axillary LN removal. Patients were assessed for BCRL stage according to the International Society of Lymphology (ISL) guidelines by a Lymphology Association of North America certified physical therapist (author PMD). Number of LNs removed, surgical side, time post-surgery, and radiation and chemotherapy treatment were recorded.

LN localization and anatomical imaging

A multi-step localization process was applied to enable identification of multiple axillary LNs per subject. Volunteers were positioned supine and scanned at 3.0T (Philips Achieva, Best, The Netherlands) using body coil transmission and 16-channel torso coil reception. A torso coil was chosen to achieve bilateral coverage of the right and left axilla.

First, a large field-of-view (FOV)=520×424×192 mm^3 was prescribed spanning the clavicle to below the mammary fold in the head-foot direction and spanning bilateral axillary regions in the left-right direction (Figure 1A). Proximity of axillary LNs was identified using a diffusion-weighted imaging with background suppression sequence (DWIBS, TR/TE=7755/53 ms, EPI-factor=71, b-value=800 s/mm^2; duration=2.7 min). A maximum intensity projection image was reconstructed from 35 slices at an acquired spatial resolution=1.6×1.6×5.5 mm^3 (Figure 1B). The DWIBS projections were used solely for planning purposes and to localize LNs, and this sequence was followed by higher spatial resolution anatomical imaging. Guided by the DWIBS reconstruction, multi-point Dixon imaging was applied (dual-echo per TR=3.5 ms, TE_1=1.15, TE_2=2.3 ms, 3D gradient echo readout; duration=18s) over the same FOV to localize LNs at a spatial resolution of 0.9×0.7×2.5 mm^3 (Figures 1C,D). Finally, the right and left axillary regions were imaged separately using a reduced FOV (180×180×50 mm^3, Figure 1E) centered on the LNs to achieve higher spatial resolution imaging with the following sequences: (i) T_2-weighted with fat-suppression (spectral attenuated inversion recovery, SPAIR, TR/TE=3500/60 ms, spatial

resolution=0.3×0.3×5 mm^3); (ii) T_1-weighted (TR/TE=991/15 ms, spatial resolution=0.54×0.54×5.5 mm^3); and (iii) T_1-weighted with fat-suppression (spectral presaturation with inversion recovery, SPIR, TR/TE=899/15 ms, spatial resolution=0.54×0.54×5.5 mm^3). Duration for the total localization protocol, including bilateral high spatial resolution scans, was approximately 25 minutes.

Quantitative relaxation time mapping of LNs

Quantitative relaxation time mapping was performed bilaterally in a volume centered on the LNs (identified as above) with FOV=520×424×50 mm^3, spatial resolution=1.8×1.5×5.5 mm^3, slices=9. T_2 mapping was achieved using a multi-echo turbo-spin-echo sequence (TE=9–189 ms, TE-interval=12 ms, TR=4000 ms) identical to previously reported[12]. T_1 mapping was achieved using the multi-flip angle (flip angle=20, 40, 60 degrees, TR/TE = 100/4.6 ms) method[13] and a 3D gradient echo readout over an identical FOV. To correct for flip angle inefficiency, a B_1 map was acquired using a dual-TR approach (TR_1=30 ms, TR_2=130 ms, flip angle=60 degrees) with identical readout, FOV, and gain settings as the multi-flip angle sequence.

Relaxation time and B_1 efficiency maps were calculated using custom routines in Matlab (v2015, Mathworks, Natick, MA). Briefly, a voxel-wise array of signal intensity from 16 echoes was fit to a mono-exponential decay function using a constrained fitting routine and the characteristic time constant was taken as the T_2 value[14]. T_1 maps were calculated by plotting voxel-wise $S_{\theta nom}/sin(\theta_{abs})$ *vs.* $S_{\theta nom}/tan(\theta_{abs})$, for which the $slope = e^{-TR/T_1}$. Here, $S_{\theta nom}$ is the acquired signal intensity at a nominal flip angle (20, 40, or 60 degrees), and θ_{abs} is the product of the nominal flip angle and B_1 efficiency ratio calculated using the standard method presented by Yarnykh *et al.*[15]. Voxel-wise T_1 was calculated from the logarithm of the slope.

Segmentation

Identification of axillary LNs was guided by the high spatial resolution T_2-weighted fat-suppressed (T_2-SPAIR) images; vasculature that could be traced through successive slices to the brachial or thoracodorsal arteries was excluded from analysis. The lengths of the short-axis and long-axis of LNs were measured on T_2-SPAIR images. LN substructures (Figure 2**;** cortex and hilum) were identified manually and segmented separately from the corresponding T_1-weighted (TR=30 ms) and T_2-weighted (TE=18 ms) images acquired for relaxometry calculations (see supplemental Figure). Regions were identified separately on T_1-weighted and T_2-weighted images to reduce potential error associated with the volunteer moving between scans. At least two LNs were segmented from each axillary region for each subject.

Simulations and contrast optimization

The first component of this work was to utilize the measured T_1 and T_2 values to generate optimal protocol parameters for visualizing lymphatic system contrast. Next, T_1 saturation recovery and T_2 decay curves were simulated based on Bloch equation solutions at equilibrium for the tissues of interest, using the measured time constants. For completeness, lymphatic fluid magnetization was simulated using relaxation times of *in vitro* human

lymphatic fluid at 3.0T[14]. Simulated magnetization of blood utilized a median value of the range reported in the literature at 3.0T, where T_1 ranges from 1600 – 1900 ms, and T_2 ranges from 96 – 122 ms, depending on the oxygenation and hematocrit levels[16–18]. Magnetization in the arm muscle (shoulder girdle and deltoid musculature) and periscapular fat tissues were simulated based on previously-published measurements in healthy controls[12].

Parameters for optimal contrast were determined as the maximum difference in simulated longitudinal magnetization (M_z) recovery or transverse magnetization (M_{xy}) decay between two tissues of interest. The optimal TR/TE parameters determined from simulations were evaluated in an example subject during a single scan session. T_2-weighted SPAIR, T_1-weighted, and T_1-weighted SPIR sequences were applied with various combinations of TR/TE, while keeping all other acquisition parameters (i.e., FOV, flip angle, and readout scheme) identical.

Statistical methods

Following the above T_1 and T_2 quantification procedures, a secondary objective was to understand whether relaxation times varied between healthy volunteers and patients with BCRL. First to understand effects in healthy controls, a multiple linear regression model was applied to evaluate the dependence of LN cortex relaxation times on age and BMI, and subject number as a covariate was included to control for multiple measurements in each subject. Second, to understand differences between control and patient values, a Mann-Whitney U-test was applied to evaluate hypothesized differences in relaxation times of the LN cortex and hilum, with a Bonferroni-corrected two-sided $p<0.025$ required for significance (two comparisons). This analysis was applied to evaluate LN cortex T_1 asymmetry (the ratio of T_1 relaxation in the LN cortex from the dominant vs. contralateral sides of controls, and surgical vs. contralateral sides of BCRL patients), with a Bonferroni-corrected two-sided $p<0.025$ required for significance (two comparisons). In patients with BCRL, a multiple linear regression model was used to evaluate the dependence of cortex T_1 asymmetry on BCRL stage, time since surgery, and number of LNs removed. Finally, a mixed multiple linear regression model was used to evaluate whether cortex T_1 asymmetry predicted disease status, either control or BCRL, considering covariates of age and BMI. Regression analyses required a two-sided significance level of 0.05. Quantified study metrics are reported as mean ± standard deviation.

Results

Lymph node identification

In total, 213 axillary LNs were identified for segmentation. In healthy volunteers, 105 axillary LNs were identified on T_1 maps (54 LNs from the dominant axilla, and 51 LNs from contralateral axilla) from which 105 LN cortex and 45 LN hilum regions were segmented. 90 axillary LNs were identified on T_2 maps (42 LNs from the dominant axilla, and 48 LNs from the contralateral axilla), from which 90 cortex and 51 hilum regions were segmented. In patients with BCRL, 108 axillary LNs were identified on T_1 maps (53 LNs from the surgical axilla, and 55 LNs from the contralateral axilla), from which 108 LN cortex and 20 LN hilum regions were segmented. 108 axillary LNs were identified on T_2

maps in patients with BCRL (47 LNs from the surgical axilla, and 61 LNs from the contralateral axilla), from which 108 cortex and 19 hilum regions were segmented. The mean±standard deviation (min, max) values of the LN short-axis was 6.9±1.5 (4.7, 11.1) mm and long-axis was 11.1±2.7 (6.2, 16.9) mm.

Relaxation times in healthy volunteers

The relaxation times of LN substructures in healthy volunteers were: T_1 cortex=1435±391 ms, T_1 hilum=714±123 ms; T_2 cortex=102±12 ms, and T_2 hilum=119±21 ms (Table I). A multiple linear regression analysis of T_1 relaxation of the LN cortex in healthy volunteers revealed a significant inverse correlation with age (model coefficient = −7.3, p=0.03), and no significant correlation with BMI (model coefficient = 1.1, p=0.83). The T_2 relaxation time of the cortex was not significantly correlated with age (model coefficient = −0.19, p=0.07) or BMI (model coefficient = 0.15, p=0.42). T_1 relaxation of the LN hilum in healthy volunteers revealed no significant correlation with age (model coefficient = −1.5, p=0.38), or BMI (model coefficient = 2.7, p=0.34). The T_2 relaxation time of the hilum was significantly correlated with BMI (model coefficient = 0.93, p=0.02) and was not significantly correlated with age (model coefficient = −0.33, p=0.19).

Simulations and LN imaging parameters

The relaxation times in the LN cortex and hilum were used to simulate evolution of water magnetization in these structures (Figure 3). Based on measured relaxation times, optimized parameters for 3.0T MRI visualization of axillary LN substructures using a T_2-weighted fat-suppressed sequence (Figure 4) and a T_1-weighted sequence with and without fat suppression (Figure 5**)** were generated. Equilibrium magnetization contrast between the LN cortex and hilum was found optimal for a T_2-weighted fat-suppressed (TE=60 ms) and a T_1-weighted (TR=580) sequence. Contrast consistent with efferent and afferent vasculature associated with axillary LNs was demonstrated for a T_2-weighted fat-suppressed (TE=121 ms) and a T_1-weighted fat-suppressed (TR=1328 ms) sequence.

BCRL participant demographics

Patients with BCRL received sentinel LN biopsy or axillary LN dissection or removal (60% on their dominant side), radiation to the surgical side (80% received), and all received chemotherapy (30% with neoadjuvant treatment). The chemotherapy regimen consisted primarily of paclitaxel (80% of subjects), cyclophosphamide (55% of subjects), and doxorubicin (50% of subjects). All subjects had concluded their chemotherapy and radiation regimen at least six months prior to imaging (mean time since surgery=4.9 years). Patients had the following clinical features: BCRL stage=1.4±0.7 (range=0–2), and number of LNs removed=14.7±8.1 (range=1–27). A summary of patient characteristics is provided in Table II.

Relaxation times in patients with BCRL

The relaxation times of LN substructures in patients with BCRL in the surgical axilla were: T_1 cortex=1541±431 ms, T_1 hilum=680±190 ms, T_2 cortex=105±22 ms, and T_2 hilum=94±9

ms. The relaxation times in the contralateral axilla were: T_1 cortex=1230±386 ms, T_1 hilum=679±86 ms, T_2 cortex=105±16 ms, and T_2 hilum=114±24 ms.

Control and patient LN relaxation time comparisons

In controls, relaxation times were not significantly different when comparing dominant and contralateral sides: dominant T_1 cortex=1441±422 ms, contralateral T_1 cortex=1428±359 ms (p=0.87); dominant T_2 cortex=100±12 ms, contralateral T_2 cortex=104±13 ms (p=0.19). BCRL patients had significantly reduced T_1 relaxation of the LN cortex in the contralateral axilla compared to the surgical axilla (p<0.001), and compared to bilateral values from controls (p<0.01, Figure 6A). BCRL patients had significantly greater T_1 asymmetry of the LN cortex (p<0.01, Figure 6B).

In patients, a multiple linear regression model yielded a significant dependence of cortex T_1 asymmetry on BCRL stage (model coefficient = 0.29, p=0.006) and time since surgery (model coefficient = 0.052, p<0.001), and a trend for a dependence on number of LNs removed (model coefficient = 0.016, p=0.07). T_1 asymmetry of the LN cortex was found to discriminate patient versus control groups (model coefficient = −0.35, p=0.004) when separately accounting for age (model coefficient = −0.003, p=0.52) and BMI (model coefficient = −0.004, p=0.65) in the regression analysis. Fewer identifiable LN hilum regions in patients prevented the hilum from being rigorously evaluated statistically.

Discussion

We report 3.0T magnetic resonance relaxation time constants for the first time from 213 human axillary LNs (cortex and hilum) from healthy adults and patients with unilateral BCRL. In healthy adults, T_1 relaxation times of LN substructures were 1435±391 ms and 714±123 ms for cortex and hilum, respectively. T_2 relaxation times were 102±12 ms and 119±21 ms for cortex and hilum, respectively. Optimal contrast between LN cortex and hilum was demonstrated using a T_2-weighted fat-suppressed sequence (TR/TE=3500/60 ms) and a T_1-weighted sequence (TR/TE=580/15 ms). Contrast consistent with lymphatic vasculature was demonstrated using a T_2-weighted fat-suppressed sequence (TR/TE=3500/121 ms) and a T_1-weighted sequence (TR/TE=1328/15 ms). These values can be utilized to inform optimal LN imaging protocols, as well as to enable functional imaging of LNs using many sequences that require quantitative knowledge of relaxation times (e.g., spin labeling[19] and molecular imaging[20]).

Study findings demonstrate that T_1 asymmetry of the LN cortex between affected and contralateral axilla varies between controls and patients with BCRL. Further, the degree of asymmetry of relaxation times provide discriminatory capacity for distinguishing patients from controls that is not apparent from traditional external risk factors for lymphedema such as age, BMI, and number of LNs removed during surgery. MR relaxometry can be performed in feasible clinical scan times (3–4 minutes for T_1 and T_2 mapping each at the proposed spatial resolution) at 3.0T MRI and, while limited to applications in LNs with axis lengths greater than approximately 1.5 mm, may provide a biomarker for unilateral lymphedema disease status.

Anatomical features of axillary lymphatics

Axillary LNs are surrounded by axillary adipose tissue, and are associated with a rich venolymphatic vascular network through the axilla, with intimate association between lymph and blood. A comparison of measured parameters in the LN cortex and axillary tissues demonstrates that the LN cortex has a longer T_1 than fat, and a similar T_1 compared to muscle; T_1 and T_2 are also similar between the LN cortex and blood. While this was previously unknown, the result is not surprising as the LN cortex is highly perfused[19], and has a high degree of cellularity similar to muscle tissue. LNs can be sufficiently distinguished from muscle because of their location, however they may be difficult to distinguish from blood vessels based on relaxation times alone. Cortex T_1 values (1435±391 ms) are in the range of 3.0T venous and arterial blood (1400–1900 ms; for a typical hematocrit of 0.28–0.44)[16–18]. Structures must be tracked through multiple slices to confirm vascular vs. non-vascular structures.

The LN hilum has a longer T_1 than adipose tissue, as well as a longer T_2 than LN cortex. This is consistent with the heterogeneous structure of the hilum that contains lymphatic tissue, lymphatic vessels, and venous/arterial vessels. Additionally, a hypointensity was demonstrated in the hilum of an example LN using T_1-weighted imaging parameters informed by T_1 of lymphatic fluid and hilum. Related hypointense signals observed in excised LNs imaged at 7.0T correlated with activated T-cell and B-cell follicles on pathology[11, 21]. Heterogeneous LN tissue and loss of the fatty hilum may indicate metastatic disease[7, 22]. Improved visualization of LN structure may be achieved noninvasively using parameters suggested here, or by imaging at higher field strengths and spatial resolution. Applications of dynamic contrast-enhanced MRI to LN imaging for axillary nodal staging may indicate altered kinetics of metastatic nodes[23, 24], although kinetics of benign LNs can mimic those of malignant tumors as well[25]. Superparamagnetic iron oxide (SPIO) agents can achieve sensitivity of 100% and specificity of 96–98% at 3.0T[26, 27] and 1.0T[7] for nodal metastasis, and is an area of active investigation.

Lymph node relaxometry asymmetry in patients with BCRL

A sub-aim of this work was to compare LN relaxometry values from healthy adults to those from patients with BCRL. BCRL is a common co-morbidity of cancer therapy, affecting approximately 30% of breast cancer patients[28]. The etiology of BCRL is well-known resulting from the removal of one or more LNs and/or radiation therapy, that permanently alters lymphatic circulation; however the pathophysiology regarding why BCRL develops only in some patients is not well-understood. In this study, we found no difference in MR relaxation times of the remaining LNs in the surgical axilla of patients with BCRL relative to relaxation times in healthy LNs. Rather, T_1 was significantly reduced in the LN cortex of the contralateral axilla, consistent with a change in the LN microenvironment. It is unlikely that this affect is due to radiation treatments, as radiation is applied to the surgical side only (in 80% of patients in this study). Rather, reports of contralateral impairment in patients with unilateral lymphedema are possible. In a recent study of 43 patients with chronic lower limb lymphedema, 70% exhibited some form of lymphadenopathy in the contralateral limb apparent on lymphoscintigraphy[29]. In a separate study, near infrared fluorescent imaging in 18 patients with BCRL revealed lymphatic abnormalities in both limbs of patients, with

bilateral abnormalities being most prevalent in more chronic patients[30], highlighting that lymphedema secondary to cancer therapies can have a systemic influence on lymphatic function.

Our findings of significantly greater MR relaxation time asymmetry with advancing BCRL stage is primarily due to reduced T_1 of the contralateral LN cortex. This trend may indicate higher lymphatic processing and associated cellular recruitment on the contralateral side to assist with elevated processing demand of intact LNs. Lymphatic processing requires macromolecular proteins and lipids[2], which contribute to an overall reduction in T_1 relaxation. Recruitment and corresponding cell density of lymphocytes in these LNs[31] may also decrease T_1 relaxation. Additionally, systemic insufficiencies in lymphatic pumping have been reported in patients who are predisposed to lymphedema[32], and may decrease LN perfusion compared to adults with healthy lymphatic pumping capacity, or compared to the surgical axilla that experiences increased processing demand.

T_2 relaxation of the LNs was not significantly different between control and patient groups, or affected and contralateral axilla of patients. Although an increase in lymphatic fluid volume would be expected to increase T_2 relaxation of lymphoid tissue, this fluid has a heterogenous and high content of lipids, macromolecules, and immune cells which serve to decrease T_2 and may partially balance the effect of increased fluid volume. Heterogeneous effects on T_2 measurement were also recognized in the tissue of patients with lymphedema, where trends varied depending on competing effects of increased fluid volume compared to fibrosis in the affected and contralateral arms[12]. Although, measurements in the tissue should not necessarily correspond to trends in the LNs themselves, as some LNs will be highly functional and others may have lower perfusion rates[19]. As with other tissues, T_2 fractionally varies less between LN compartments than T_1, and therefore it is possible that T_2-weighted sequences are less capable of identifying small differences in microenvironment compared to T_1-weighted sequences.

Clinical applications of noninvasive imaging of lymphatic tissue

Abilities to identify the presence of clinically-relevant residual LN disease through noninvasive MRI without imposing the need for LN biopsy or complete lymphadenectomy could reduce the requirement for current surgical approaches used for cancer staging and cancer treatment[33, 34]. Surgical interventions permanently disrupt the lymphatic circulation and are unnecessary when no nodal disease is present[35], yet may result in substantial quality of life issues for survivors[36]. Further, an imaging signature of LN metastasis and lymphatic vasculature would be useful to validate targeted delivery and efficacy of immunomodulators or chemotherapeutics to LNs[37] where anatomical indicators alone are incomplete[25].

This presents a need for the development of molecular and functional imaging methodologies to target LNs and vasculature, which exploit the unique physical properties of lymphatic fluid and flow. Lymphatic fluid is rich in large macromolecular proteins[38]. Amide proton transfer (APT) chemical exchange saturation transfer imaging (CEST) has shown abilities to detect contrast consistent with proteinaceous lymph stasis in the upper extremities of patients with secondary lymphedema[20]. However, improved APT-CEST contrast and quantitation accuracy can be extended with knowledge of MR relaxation times

of lymphatic tissue. Specifically, the CEST signal enhancement due to proton transfer depends partly on the T_1 and T_2 relaxation of water in the tissue of interest[39]. Here we have measured longer T_1 relaxation in the LN hilum compared to skeletal fat tissue, and a longer T_2 relaxation in the LN cortex compared to muscle; these trends should contribute to enhanced APT-CEST signal in LN tissue.

Advanced MRI methods that can be utilized to measure lymph flow velocity and perfusion in LNs can employ spin-labeling techniques as well. Spin-labeling has been applied to evaluate lymphatic flow and demonstrated slower lymphatic flow into axillary LNs of healthy volunteers under conditions of cuff-induced lymphatic steno-occlusion and in patients with secondary lymphedema[14]. LN perfusion in spin labeling experiments is assessed based on the extent of T_1-weighted signal attenuation in the LN secondary to blood water labeling and exchange. As such, knowledge of both blood-water T_1 and LN T_1 is required.

The unique T_2 relaxation time of lymphatic tissue can be exploited using MRI methods sensitive to long T_2 species. Specifically, a long turbo-spin-echo sequence with multiple refocusing pulses will be sensitized to spins with long T_2 decay and slower velocities such that the transverse signal is preserved. We have implemented a preliminary version of this sequence to provide a non-contrast MR lymphangiography method based on measured T_2 relaxation of lymphatic fluid, and we have demonstrated its sensitivity to subjects with clinical lymph stasis and enlarged vessels[40]. LNs are typically not visualized in MR lymphangiograms using long TSE sequences due to the relatively shorter T_2 relaxation compared to lymphatic fluid. This study provides examples of vessel structures associated with LNs that can be visualized with acquisition parameters optimized for LN T_1 and T_2. These parameters may also have relevance for improving visualization of lymphatic vessels in recently proposed lymphangiography sequences.

Limitations

First, our aim was to measure *in vivo* LN relaxation times, and cortex and hilum were manually delineated based on knowledge of LN anatomy. To ensure accurate segmentation, only larger LNs on the order of the spatial resolution of our measurements (approximately 5 mm in minimum cross-sectional diameter, corresponding to at least 4 voxels) were included, and sub-regions identified only when apparent in typically reniform lymph nodes. While there is no reason to believe that LN T_1 and T_2 depends on LN size, this study is not capable of addressing this possibility. Abilities to apply MR relaxometry to smaller LNs are limited, and this approach should motivate the development of more sensitive MRI methods for imaging LN function and lymphatic vasculature. Second, no complementary histological study was performed here, which was prohibited by the partial study goal of characterizing LN relaxation in healthy LNs which cannot be excised without clinical indication. The relaxation times measured in excised, formaldehyde fixed healthy LNs have been reported: whole LN T_1=944±113 ms and T_2=32±2 ms)[11], and are not directly comparable to the relaxation times measured here at 3.0T, owing to inherent differences of *in vivo* and *ex vivo* water relaxation. Finally, the differences in LN relaxation between patients and controls focused on LN cortex only, as the hilum was difficult to identify in the majority of patient

LNs. This was partly attributable to the fewer number of LNs present in patients after resection and potential anatomical changes in the LNs of BCRL patients that complicate visualization of the hilum. Therefore, while we provide statistically significant differences in LN cortex between patients and controls, due to the available sample size in patients we cannot rule out the possibility that hilum differences exist between groups as well.

Conclusion

Quantitative magnetic resonance relaxation times were measured at 3.0T in axillary LN substructures, including the cortex and hilum, from healthy subjects and subjects with lymphatic processing insufficiency secondary to cancer therapies and breast cancer treatment-related lymphedema. The measurements of T_1 and T_2 relaxation times are intended to provide a necessary reference for further development of noninvasive lymphatic imaging technologies.

Supplementary Material

Refer to Web version on PubMed Central for supplementary material.

Acknowledgments

Funding: NIH/NINR 1R01NR01507901, Postdoctoral Research Fellowship from Lipedema Foundation, Lymphatic Education & Research Network, and Fat Disorders Research Society

List of abbreviations

APT:	amide proton transfer
a.u.:	arbitrary units
BCRL:	breast cancer treatment-related lymphedema
B_1:	transmit magnetic field
CEST:	chemical exchange saturation transfer
DWIBS:	diffusion-weighted imaging with background suppression
EPI:	echo-planar imaging
FOV:	field-of-view
IRB:	Institutional Review Board
ISL:	International Society of Lymphology
LN:	lymph node
MRI:	magnetic resonance imaging
M_z:	longitudinal magnetization
M_{xy}:	transverse magnetization

$S_{\theta nom}$:	acquired signal intensity at a nominal flip angle
SPAIR:	spectral attenuated inversion recovery
SPIO:	superparamagnetic iron oxide
SPIR:	spectral presaturation with inversion recovery
TE:	echo time
TR:	repetition time
T_1:	longitudinal relaxation time constant
T_2:	transverse relaxation time constant
T:	Tesla magnetic field strength
θ_{abs}:	product of the nominal flip angle and B_1 efficiency ratio

References

1. Foldi E, an Foldi M Lipedema Foldi's Textbook of Lymphology, Elsevier GmbH, Munich, Germany 2006: 417–427.
2. Ma Swartz. The physiology of the lymphatic system. Advanced Drug Delivery Reviews 2001; 50(1-2): 3–20. [PubMed: 11489331]
3. Karaman S, Detmar M. Mechanisms of lymphatic metastasis. J Clin Invest 2014; 124(3): 922–8. [PubMed: 24590277]
4. Rockson SG, Rivera KK. Estimating the population burden of lymphedema. Ann N Y Acad Sci 2008; 1131: 147–54. [PubMed: 18519968]
5. Mortimer PS, Rockson SG. New developments in clinical aspects of lymphatic disease. J Clin Invest 2014; 124(3): 915–21. [PubMed: 24590276]
6. Molenkamp BG, Vuylsteke RJ, van Leeuwen PA, Meijer S, Vos W, Wijnands PG et al. Matched skin and sentinel lymph node samples of melanoma patients reveal exclusive migration of mature dendritic cells. Am J Pathol 2005; 167(5): 1301–7. [PubMed: 16251414]
7. Memarsadeghi M, Riedl CC, Kaneider A, Galid A, Rudas M, Matzek W et al. Axillary Lymph Node Metastases in Patients with Breast Carcinomas : Assessment with Methods : Results : Conclusion. Radiology 2006; 241(2): 367–377. [PubMed: 17057065]
8. Habermann TM, Steensma DP. Lymphadenopathy. Mayo Clin Proc 2000; 75(7): 723–32. [PubMed: 10907389]
9. Sayegh HE, Asdourian MS, Swaroop MN, Brunelle CL, Skolny MN, Salama L et al. Diagnostic Methods, Risk Factors, Prevention, and Management of Breast Cancer-Related Lymphedema: Past, Present, and Future Directions. Curr Breast Cancer Rep 2017; 9(2): 111–121. [PubMed: 28894513]
10. Moseley AL, Carati CJ, Piller NB. A systematic review of common conservative therapies for arm lymphoedema secondary to breast cancer treatment. Annals of oncology : official journal of the European Society for Medical Oncology / ESMO 2007; 18(4): 639–46.
11. Korteweg MA, Zwanenburg JJ, van Diest PJ, van den Bosch MA, Luijten PR, van Hillegersberg R et al. Characterization of ex vivo healthy human axillary lymph nodes with high resolution 7 Tesla MRI. Eur Radiol 2011; 21(2): 310–7. [PubMed: 20694817]
12. Donahue PM, Crescenzi R, Scott AO, Braxton V, Desai A, Smith SA et al. Bilateral Changes in Deep Tissue Environment After Manual Lymphatic Drainage in Patients with Breast Cancer Treatment-Related Lymphedema. Lymphat Res Biol 2017; 15(1): 45–56. [PubMed: 28323572]
13. Wang J, Qiu M, Kim H, Constable RT T1 Measurements incorporating flip angle calibration and correction in vivo. Journal of Magnetic Resonance 2006; 182: 283–292.

14. Rane S, Donahue PMC, Towse T, Ridner S, Chappell M, Jordi J et al. Clinical feasibility of noninvasive visualization of lymphatic flow with principles of spin labeling MR imaging: implications for lymphedema assessment. Radiology 2013; 269(3): 893–902. [PubMed: 23864103]
15. Yarnykh VL. Actual flip-angle imaging in the pulsed steady state: a method for rapid three-dimensional mapping of the transmitted radiofrequency field. Magn Reson Med 2007; 57(1): 192–200. [PubMed: 17191242]
16. Lu H, Clingman C, Golay X, van Zijl PC Determining the longitudinal relaxation time (T1) of blood at 3.0 Tesla. Magnetic resonance in medicine 2004; 52: 679–682. [PubMed: 15334591]
17. Zhao JM, Clingman CS, Narvainen MJ, Kauppinen RA, van Zijl PC Oxygenation and hematocrit dependence of transverse relaxation rates of blood at 3T. Magnetic resonance in medicine 2007; 58: 592–597. [PubMed: 17763354]
18. Li W, Grgac K, Huang A, Yadav N, Qin Q, van Zijl PC Quantitative theory for the longitudinal relaxation time of blood water. Magnetic resonance in medicine 2016; 76: 270–281. [PubMed: 26285144]
19. Rane S, Donahue PM, Towse T, Ridner S, Chappell M, Jordi J et al. Clinical feasibility of noninvasive visualization of lymphatic flow with principles of spin labeling MR imaging: implications for lymphedema assessment. Radiology 2013; 269(3): 893–902. [PubMed: 23864103]
20. Donahue MJ, Donahue PC, Rane S, Thompson CR, Strother MK, Scott AO et al. Assessment of lymphatic impairment and interstitial protein accumulation in patients with breast cancer treatment-related lymphedema using CEST MRI. Magn Reson Med 2016; 75(1): 345–55. [PubMed: 25752499]
21. Korteweg MA, Zwanenburg JJ, Hoogduin JM, van den Bosch MA, van Diest PJ, van Hillegersberg R et al. Dissected sentinel lymph nodes of breast cancer patients: characterization with high-spatial-resolution 7-T MR imaging. Radiology 2011; 261(1): 127–35. [PubMed: 21673230]
22. Mortellaro VE, Marshall J, Singer L, Hochwald SN, Chang M, Copeland EM et al. Magnetic Resonance Imaging for Axillary Staging in Patients With Breast Cancer. Journal of Magnetic Resonance Imaging 2009; 30(2): 309–312. [PubMed: 19466713]
23. Rahbar H, Conlin JL, Parsian S, DeMartini WB, Peacock S, Lehman CD et al. Suspicious axillary lymph nodes identified on clinical breast MRI in patients newly diagnosed with breast cancer: can quantitative features improve discrimination of malignant from benign? Acad Radiol 2015; 22(4): 430–8. [PubMed: 25491740]
24. Kvistad KA, Rydland J, Smethurst HB, Lundgren S, Fjosne HE, Haraldseth O. Axillary lymph node metastases in breast cancer: preoperative detection with dynamic contrast-enhanced MRI. European Radiology 2000; 10(9): 1464–1471. [PubMed: 10997438]
25. Ecanow JS, Abe H, Newstead GM, Ecanow DB, Jeske JM. Axillary staging of breast cancer: what the radiologist should know. Radiographics 2013; 33(6): 1589–612. [PubMed: 24108553]
26. Motomura K, Ishitobi M, Komoike Y, Koyama H, Noguchi A, Sumino H et al. SPIO-Enhanced Magnetic Resonance Imaging for the Detection of Metastases in Sentinel Nodes Localized by Computed Tomography Lymphography in Patients with Breast Cancer. Annals of Surgical Oncology 2011; 18(12): 3422–3429. [PubMed: 21607775]
27. Motomura K, Izumi T, Tateishi S, Tamaki Y, Ito Y, Horinouchi T et al. Superparamagnetic iron oxide-enhanced MRI at 3 T for accurate axillary staging in breast cancer. 2016: 60–69.
28. DiSipio T, Rye S, Newman B, Hayes S. Incidence of unilateral arm lymphoedema after breast cancer: a systematic review and meta-analysis. The Lancet. Oncology 2013; 14(6): 500–15. [PubMed: 23540561]
29. de Almeida CA, Lins EM, Brandao SCS, Ferraz AAB, Pinto FCM, de Barros Marques SR. Lymphoscintigraphic abnormalities in the contralateral lower limbs of patients with unilateral lymphedema. J Vasc Surg Venous Lymphat Disord 2017; 5(3): 363–369. [PubMed: 28411704]
30. Aldrich MB, Guilliod R, Fife CE, Maus EA, Smith L, Rasmussen JC et al. Lymphatic abnormalities in the normal contralateral arms of subjects with breast cancer-related lymphedema as assessed by near-infrared fluorescent imaging. Biomed Opt Express 2012; 3(6): 1256–65. [PubMed: 22741072]

31. Olszewski WL, Engeset A, Romaniuk A, Grzelak I, Ziolkowska A. Immune cells in peripheral lymph and skin of patients with obstructive lymphedema. Lymphology 1990; 23(1): 23–33. [PubMed: 2352440]
32. Stanton AW, Modi S, Mellor RH, Levick JR, Mortimer PS. Recent advances in breast cancer-related lymphedema of the arm: lymphatic pump failure and predisposing factors. Lymphat Res Biol 2009; 7(1): 29–45. [PubMed: 19302022]
33. Qiu SQ, Aarnink M, van Maaren MC, Dorrius MD, Bhattacharya A, Veltman J et al. Validation and update of a lymph node metastasis prediction model for breast cancer. Eur J Surg Oncol 2018; 44(5): 700–707. [PubMed: 29449047]
34. McCready DR, Yong WS, Ng AK, Miller N, Done S, Youngson B. Influence of the new AJCC breast cancer staging system on sentinel lymph node positivity and false-negative rates. J Natl Cancer Inst 2004; 96(11): 873–5. [PubMed: 15173271]
35. Pilewskie M, Jochelson M, Gooch JC, Patil S, Stempel M, Morrow M. Is Preoperative Axillary Imaging Beneficial in Identifying Clinically Node-Negative Patients Requiring Axillary Lymph Node Dissection? J Am Coll Surg 2016; 222(2): 138–45. [PubMed: 26711795]
36. Fracheboud J, Otto SJ, van Dijck JA, Broeders MJ, Verbeek AL, de Koning HJ et al. Decreased rates of advanced breast cancer due to mammography screening in The Netherlands. Br J Cancer 2004; 91(5): 861–7. [PubMed: 15292936]
37. Oliver G, Detmar M. The rediscovery of the lymphatic system: Old and new insights into the development and biological function of the lymphatic vasculature. Genes and Development 2002; 16: 773–783. [PubMed: 11937485]
38. Hansen KC, D'Alessandro A, Clement CC, Santambrogio L. Lymph formation, composition and circulation: a proteomics perspective. Int Immunol 2015; 27(5): 219–27. [PubMed: 25788586]
39. Zaiss M, Bachert P. Chemical exchange saturation transfer (CEST) and MR Z-spectroscopy in vivo: a review of theoretical approaches and methods. Phys Med Biol 2013; 58(22): R221–69. [PubMed: 24201125]
40. Crescenzi R, Donahue PM, Hartley KG, Desai AA, Scott AO, Braxton V et al. Lymphedema evaluation using noninvasive 3T MR lymphangiography. J Magn Reson Imaging 2017.

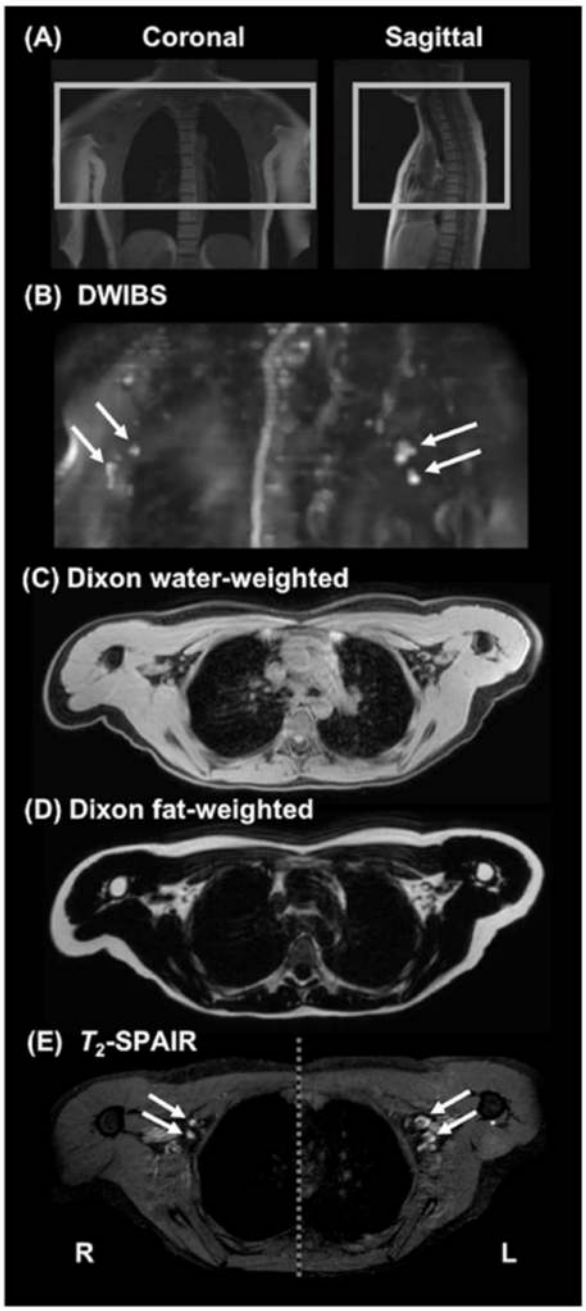

Figure 1. Lymph node identification at 3.0T.

(A) Slice planning is achieved over a bilateral field-of-view. (B) Axillary lymph nodes are located using a DWIBS maximum intensity projection (white arrows depict axillary lymph nodes). Transverse imaging is centered over axillary lymph nodes. (C-D) The multi-point Dixon method is used to acquire anatomical contrast from fat and muscle tissues; axillary lymph node cortex is hyperintense on the water-weighted image while the fatty hilum is hyperintense on the fat-weighted image. (E) High spatial resolution T_2-weighted imaging

with fat-suppression (T_2-SPAIR) is used to visualize the lymph node cortex. Two axillary lymph nodes in the right (R) and left (L) axillae (white arrows) are displayed.

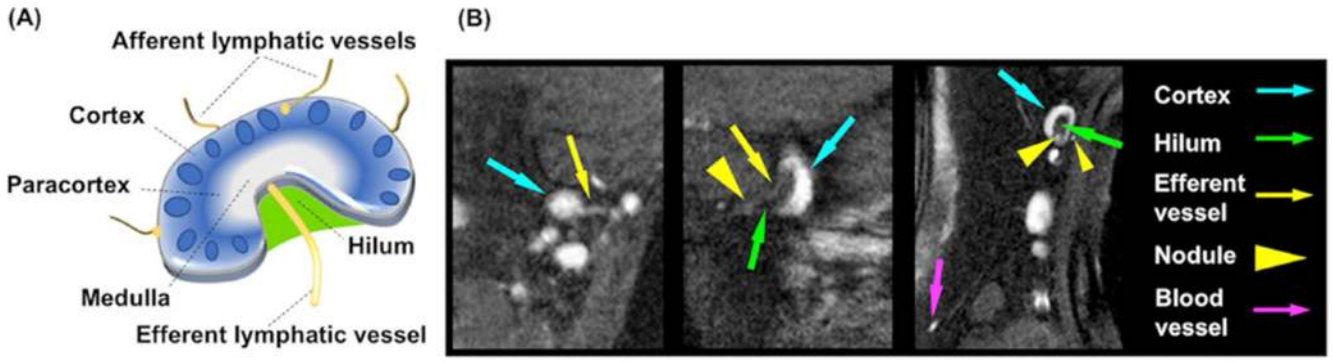

Figure 2. Axillary lymph node substructures visualized *in vivo* at 3.0T MRI.

(A) The schematic of a lymph node demonstrates afferent vessels that enter the outer cortex (blue) rich in B-cell follicles (blue circles), an inner paracortex (faded blue) and medullary region (gray), and an efferent vessel that exits the fatty hilum (green). Vessels that localize on the cortex may appear as nodules at their intersection. (B) Images of healthy axillary lymph nodes and substructures visible *in vivo* were acquired at 3.0T using a T_2-weighted fat-suppressed sequence, including lymph nodes with different orientation (three panels). Contrast consistent with vessels can be discerned by considering longitudinal orientation on multiple imaging planes.

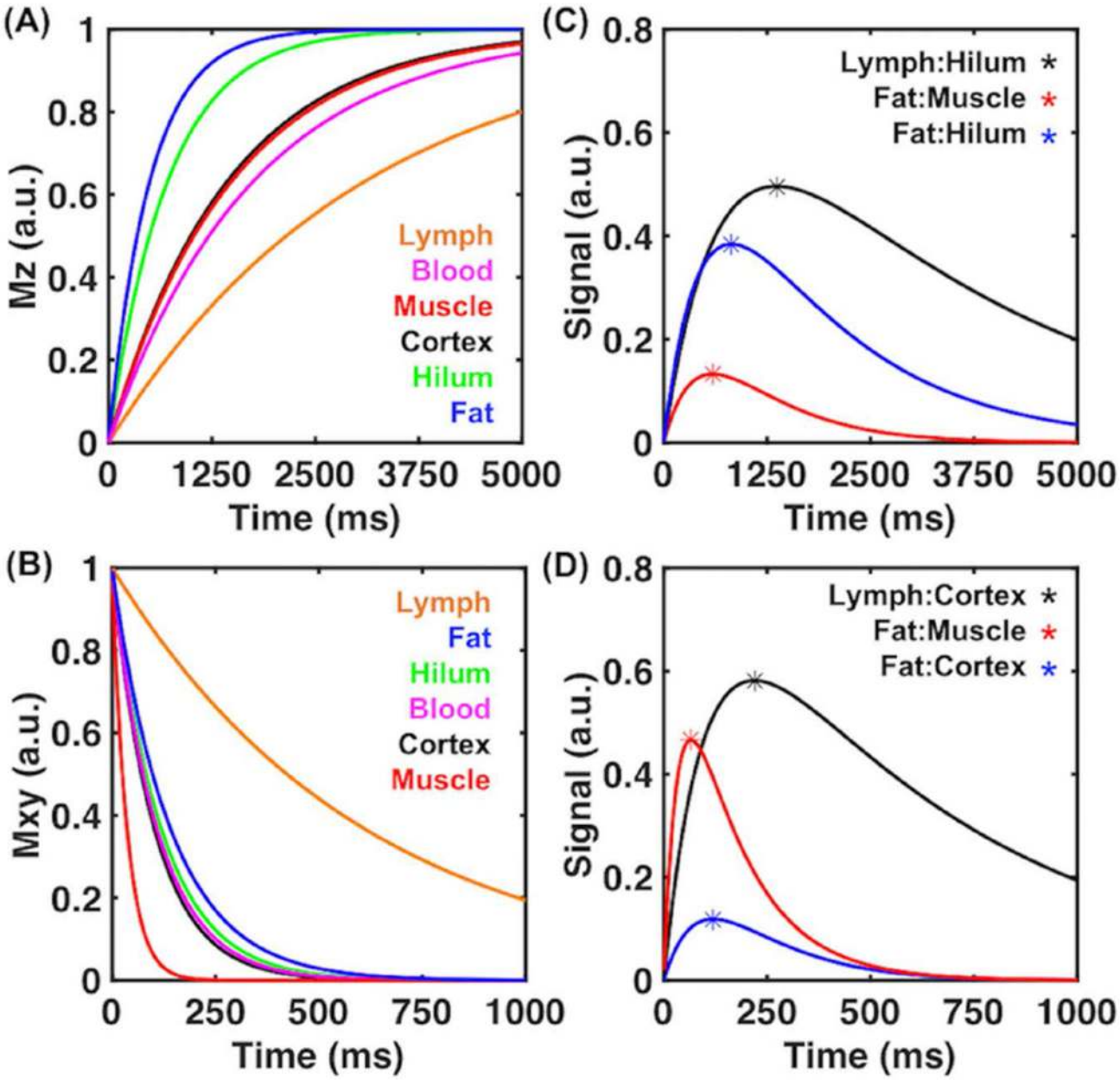

Figure 3. Simulated magnetization and signal contrast using measured T_1 and T_2 relaxation times of lymph node substructures and axillary tissues.

(A-B) Simulations from Bloch equation solutions for longitudinal (Mz) and transverse (Mxy) magnetization (arbitrary units, a.u.) of tissues using T_1 and T_2 characteristic time constants measured in this study or reported in the literature (blood and lymphatic fluid). (C-D) Simulated contrast between combinations of two tissues of interest (tissue1:tissue2). The optimal TR and TE are defined at the maximum difference between two recovery or decay curves, respectively. Tissue combinations were chosen with the following rationale: fat vs. muscle to represent the typical musculoskeletal imaging protocol; fat vs. nodal cortex or

hilum to discern lymph node substructures from adipose tissue; and lymphatic fluid vs. nodal cortex or hilum to discern lymphatic vasculature from the cortex or hilum.

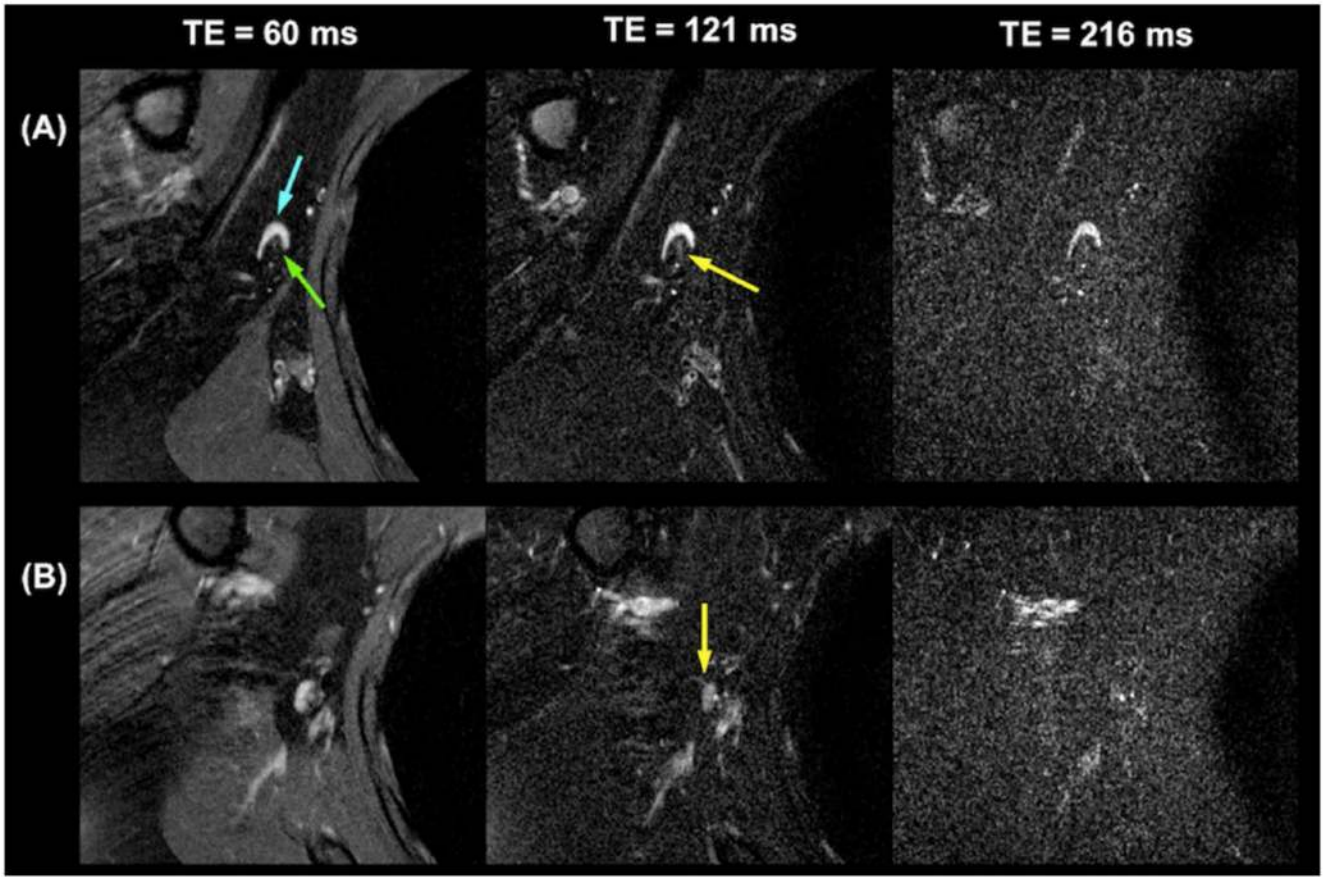

Figure 4. T_2-weighted imaging with fat suppression of an axillary lymph node at varying TEs.
An array of TE values using a T_2-weighted sequence with fat suppression (TR=3500 ms) presents different contrast among axillary tissues. (A) The lymph node cortex (blue arrow) demonstrates maximum contrast relative to the hilum (green arrow) at TE=60 ms. Contrast consistent with an efferent vessel exiting the cortex is visualized at TE=121 ms (yellow arrow). (B) The example lymph node is a round node without a visible hilum region. Contrast consistent with an afferent vessel is demonstrated at TE=121 ms (yellow arrow).

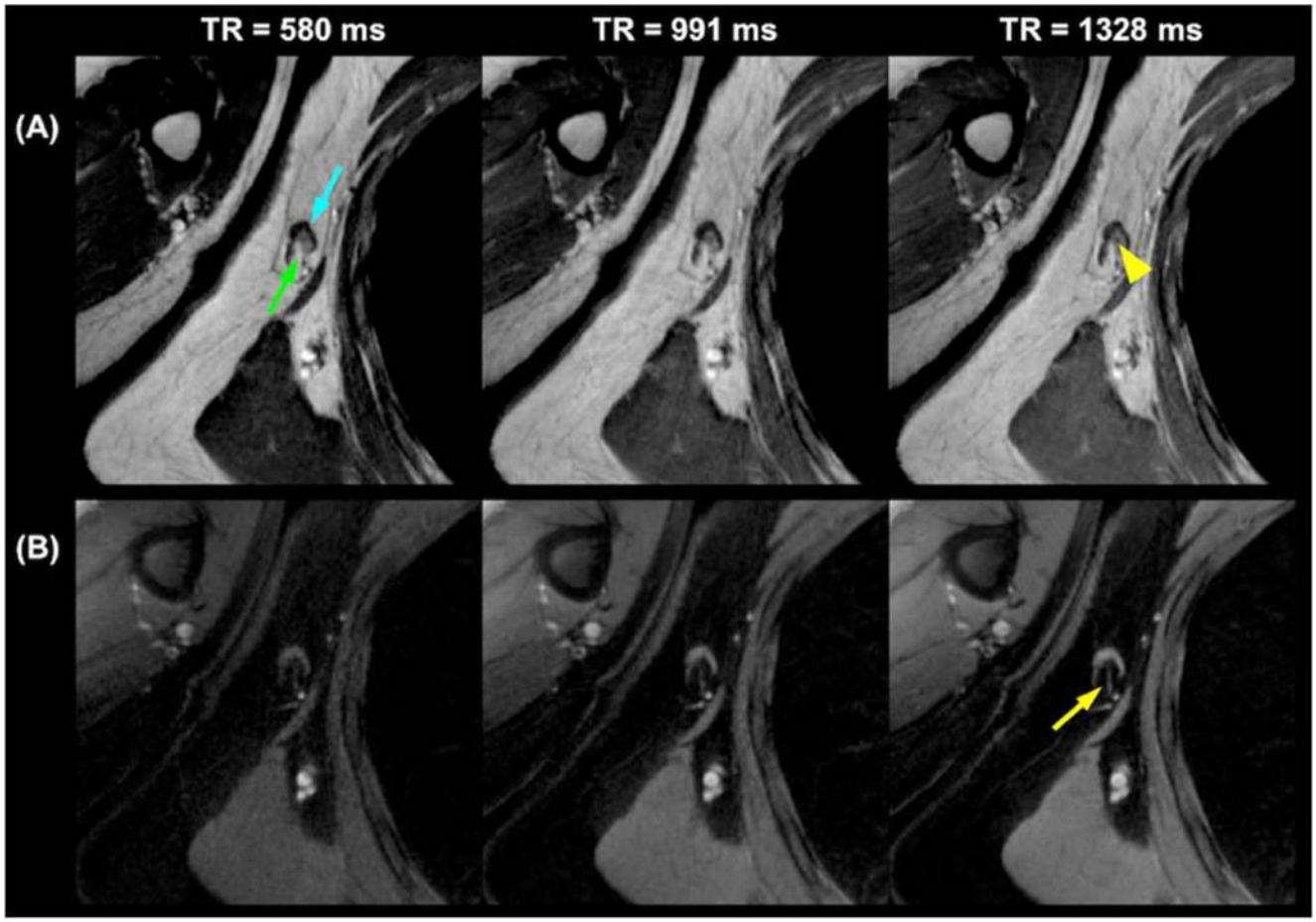

Figure 5. T_1-weighted imaging with and without fat suppression of an axillary lymph node at varying TRs.

An array of TR values using a T_1-weighted sequence (TE=15 ms) presents different contrast between lymphoid tissue in the axilla. (A) The example reniform lymph node has an outer cortex (blue arrow) that can be distinguished from the inner hilum (green arrow) at TR=580 ms. A hypointensity (yellow arrowhead) is also visible within the hilum at the longest TR=1328 ms. (B) T_1-weighted images with fat suppression demonstrate contrast consistent with an efferent vessel (yellow arrow) exiting the cortex through the hilum at TR=1328 ms.

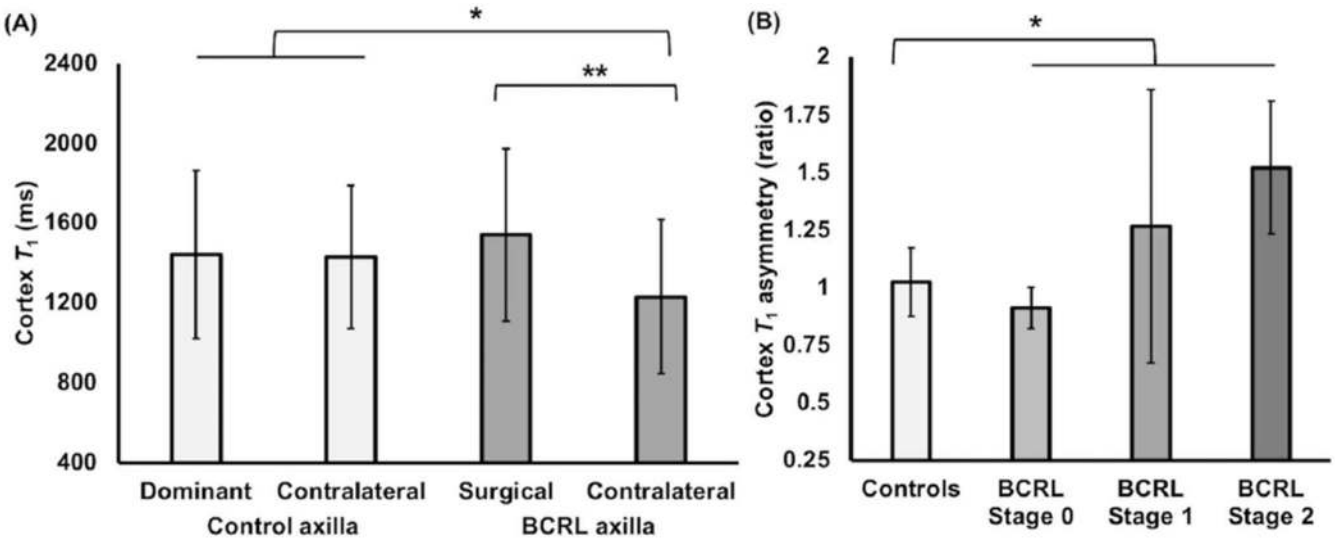

Figure 6. The T_1 relaxation time (ms) of the lymph node cortex in control participants and patients with BCRL.

(A) Lymph nodes in patients with BCRL from the contralateral axilla (n=55) have significantly lower T_1 values than those from the surgical axilla (n=53, p<0.001) or from the dominant (n=54) and contralateral sides (n=51) in female controls (p=0.002). (B) The lymph node cortex T_1 asymmetry represents the ratio of T_1 measured in the dominant vs. contralateral sides of controls, or surgical vs. contralateral sides of patients. The cortex T_1 asymmetry is significantly greater in patients with BCRL compared to controls (p=0.004). Analyses were performed using a Mann-Whitney U-test with two-sided significance *p<0.01 or **p<0.001. Error bars denote the standard deviation from the mean.

Table I.

Quantitative MR relaxation times in axillary tissues of interest at 3.0T

	T_1 (ms)	T_2 (ms)
lymph node cortex	1435 ± 391	102 ± 12
lymph node hilum	714 ± 123	119 ± 21
lymphatic fluid	3100 ± 160 †	610 ± 12 †
arm muscle	1487 ± 50	36 ± 3
periscapular fat	497 ± 178	141 ± 3
arterial blood	1750 ± 150 *	109 ± 13 **

† Rane *et al.* 2013

* Lu *et al.* 2004

** Zhao *et al.* 2007

Table II:

Demographic and clinical data from 20 enrolled patients with unilateral breast cancer treatment-related lymphedema (BCRL) of the upper extremities.

Subject ID	Age (years)	BMI (kg/m^2)	BCRL Surgical Side (R)ight=1; (L)eft=0	Number of LNs removed	Lymphedema Stage	Radiation (Yes=1; No=0)	Neo-adjuvent (Yes=1; No=0)	Adjuvent (Yes=1; No=0)	Time Since Surgery (years)
P01	55	31.0	R	22	2	Yes	No	Yes	3.0
P02	54	22.5	R	21	2	No	No	Yes	1.4
P03	44	30.7	R	1	2	No	No	Yes	4.6
P04	47	26.4	R	27	0	Yes	Yes	Yes	1.3
P05	41	34.2	R	15	1	No	Yes	Yes	0.6
P06	53	32.9	L	5	1	Yes	No	Yes	1.0
P07	48	36.7	L	18	2	Yes	No	Yes	13.2
P08	57	21.6	L	21	1	Yes	No	Yes	24.4
P09	33	30.9	R	24	2	Yes	Yes	Yes	2.0
P10	77	22.3	R	16	2	Yes	No	Yes	9.1
P11	59	25.3	R	19	1	Yes	Yes	Yes	4.3
P12	49	28.4	L	8	2	Yes	No	Yes	3.7
P13	53	25.2	R	20	1	Yes	Yes	Yes	1.9
P14	58	20.2	R	25	1	No	No	Yes	3.6
P15	58	26.5	L	12	2	Yes	No	No	6.6
P16	45	29.6	L	17	2	Yes	No	Yes	0.9
P17	51	29.3	R	14	2	Yes	Yes	No	2.2
P18	64	28.7	R	4	1	Yes	No	Yes	1.2
P19	59	36.1	L	2	1	Yes	No	Yes	2.2
P20	54	29.8	L	2	0	Yes	No	Yes	11.0
Mean	53	28.4	0.6	14.7	1.4	0.8	0.3	0.9	4.9
Standard deviation	9	4.6	0.5	8.1	0.7	0.4	0.5	0.3	5.6